UC Santa Barbara
UC Santa Barbara Previously Published Works

Title

The kagomé metals RbTi

$_3$

Bi

$_5$

and CsTi

$_3$

Bi

$_5$

Permalink

Journal

ISSN

Authors

Werhahn, Dominik
Ortiz, Brenden R
Hay, Aurland K
et al.

Publication Date

DOI

Peer reviewed

Dominik Werhahn, Brenden R. Ortiz, Aurland K. Hay, Stephen D. Wilson, Ram Seshadri
and Dirk Johrendt*

The kagomé metals RbTi$_3$Bi$_5$ and CsTi$_3$Bi$_5$

Abstract: The kagomé metals RbTi$_3$Bi$_5$ and CsTi$_3$Bi$_5$ were synthesized both as polycrystalline powders by heating the elements in an argon atmosphere and as single crystals grown using a self-flux method. The compounds crystallize in the hexagonal crystal system isotypically to KV$_3$Sb$_5$ ($P6/mmm$, $Z = 1$, CsTi$_3$Bi$_5$: a = 5.7873(1), c = 9.2062(1) Å; RbTi$_3$Bi$_5$: a = 5.773(1), c = 9.065(1) Å). The titanium atoms form a kagomé net with bismuth atoms in the hexagons as well as above and below the triangles. The alkali metal atoms are coordinated by 12 bismuth atoms and form AlB$_2$-like slabs between the kagomé layers. Magnetic susceptibility measurements with CsTi$_3$Bi$_5$ and RbTi$_3$Bi$_5$ single crystals reveal Pauli-paramagnetism and traces of superconductivity caused by CsBi$_2$/RbBi$_2$ impurities. Magnetotransport measurements reveal conventional Fermi liquid behavior and quantum oscillations indicative of a single dominant orbit at low temperature. DFT calculations show the characteristic metallic kagomé band structure similar to that of CsV$_3$Sb$_5$ with reduced band filling. A symmetry analysis of the band structure does not reveal an obvious and unique signature of a nontrivial topology.

Keywords: bismuth; DFT calculations; kagomé metals; magnetic properties; titanium

1 Introduction

The kagomé net of corner-connected triangles (Figure 1) is a common structural motif in minerals [1] and intermetallic compounds like the Laves phases [2]. It was first named by the Japanese physicist Itiro Syôzi because of its similarity to the woven patterns of bamboo baskets [3]. His work already fore-shadowed that kagomé nets may exhibit exceptional properties since he showed that, unlike in square and hexagonal nets, antiferromagnetism is highly frustrated within the kagomé net.

Later it turned out that its inherent spin frustration can indeed result in exceptional electronic or magnetic ground states. One of them is the quantum spin liquid (QSL), a theoretical concept introduced by P. W. Anderson who proposed it as an alternative to the antiferromagnetic Néel state [4]. Magnetic order in kagomé lattices can be induced by quantum fluctuations, a special case of order from disorder [5]. The theoretical concept was further developed under the motivation to explain high-T_c superconductivity [6]. However, the experimental realization of the QSL turned out to be difficult, and despite many extensive studies [7–14], the question as to whether it exists or not remains under debate [15]. Another peculiarity is that itinerant (delocalized) electrons on a kagomé lattice form a Dirac semimetal like graphene [16]. Therefore kagomé lattices have attracted much attention as a base for the realization of correlated and topological quantum states like charge fractionalization [17], density waves [16] and superconductivity [18]. The recently discovered kagomé metals AV$_3$Sb$_5$ (A = K, Rb, Cs) [19] showed particularly rich physics like unconventional chiral charge order with topological band structures [20], superconducting ground states [21, 22] as well as a giant extrinsic anomalous Hall effect [23]. It is quite interesting to examine the properties of the KV$_3$Sb$_5$-type compounds as a function of the band filling. Hole doping with tin revealed increasing superconducting T_c's during rapid suppression of the charge density waves in KV$_3$Sb$_{5-x}$Sn$_x$ ($0 \leq x \leq 1$) [24] and double-dome superconductivity in CsV$_3$Sb$_{5-x}$Sn$_x$ ($0 \leq x \leq 1$) [25]. Apparently the properties change strongly with the electron count, and although other variants of the AM$_3$X$_5$ family are predicted, only the vanadium antimonides AV$_3$Sb$_5$ are currently known [26]. During a systematic investigation, we discovered RbTi$_3$Bi$_5$ and CsTi$_3$Bi$_5$, which crystallize in the KV$_3$Sb$_5$-type structure and have a significantly reduced band filling. Here we present the synthesis, single-crystal growth, crystal structure, basic magnetic and transport properties as well as the electronic band structure of the new members of the KV$_3$Sb$_5$-type family.

*Corresponding author: Dirk Johrendt, Department Chemie, Ludwig-Maximilians-Universität München, Butenandtstraße 5–13, 81377 München, Germany, E-mail: johrendt@lmu.de
Dominik Werhahn, Department Chemie, Ludwig-Maximilians-Universität München, Butenandtstraße 5–13, 81377 München, Germany
Brenden R. Ortiz, Aurland K. Hay, Stephen D. Wilson and Ram Seshadri, Materials Department, Materials Research Laboratory and California Nanosystems Institute, University of California Santa Barbara, Santa Barbara, CA 93106, USA
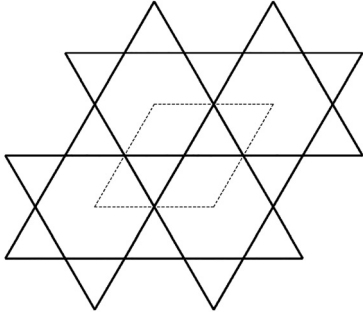
Figure 1: The four-connected kagomé net of corner-sharing triangles (plane group *p6mm*).

2 Results

2.1 Synthesis and crystal structure

Polycrystalline samples of RbTi$_3$Bi$_5$ and CsTi$_3$Bi$_5$ form by heating stoichiometric mixtures of the elements at $T = 600\,°C$ in alumina crucibles welded in silica tubes under an atmosphere of purified argon. The resulting black powders are extremely sensitive to air and decompose rapidly. Single crystals of RbTi$_3$Bi$_5$ and CsTi$_3$Bi$_5$ were synthesized using a self-flux method published previously [27]. Crystals form as hexagonal plates with typical dimensions of up to $10 \times 10 \times 0.25$ mm^3. They are malleable, readily exfoliated and extremely sensitive to air and water. A small single crystal suitable for X-ray diffraction was selected from the CsTi$_3$Bi$_5$ powder sample and sealed in a glass capillary under argon atmosphere. The structure was solved and refined in the hexagonal space group *P6/mmm* which resulted in the crystal structure isotypic to KV$_3$Sb$_5$. The structure of RbTi$_3$Bi$_5$ was refined from X-ray powder data using the atom coordinates of CsTi$_3$Bi$_5$ as starting parameters (RbTi$_3$Bi$_5$: $a = 5.773(1)$, $c = 9.065(1)$ Å, $z_{Bi2} = 0.2335(4)$, $R_p = 0.025$, GoF = 0.961). The main results of the single-crystal structure determination are compiled in Tables 1–3. X-ray powder diffraction patterns of both compounds contain small amounts (~1–3 wt%) of the cubic Laves phases RbBi$_2$ and CsBi$_2$ as the only impurity, respectively (Figure 2). Due to the large X-ray absorption, the powders in the capillaries have been diluted with ground silica, which adds a diffuse background.

Figure 3 shows the crystal structure of CsTi$_3$Bi$_5$. The titanium atoms form a planar kagomé net ($d_{Ti-Ti} = 2.8937(2)$ Å) with bismuth atoms in the centers of the hexagons ($d_{Ti-Bi2} = 2.8937(2)$ Å, Figure 3a) as well as above and below the triangles ($d_{Ti-Bi1} = 2.929(1)$ Å, Figure 3b). These bismuth atoms form face-sharing hexagonal prisms around the cesium atoms ($d_{Cs-Bi1} = 3.999(1)$ Å Figure 3c) that leads to

Table 1: Crystallographic data of CsTi$_3$Bi$_5$.

Empirical formula	CsTi$_3$Bi$_5$
Color and habitus	Black plate
Molecular mass, g mol^{-1}	1321.51
Crystal size, mm^3	$0.12 \times 0.12 \times 0.04$
Crystal system	Hexagonal
Space group	*P6/mmm* (no. 191)
a, Å	5.7873(3)
c, Å	9.2062(6)
V, Å^3	267.03(3)
Z	1
ρ_{calcd}, g cm^{-3}	8.22
μ(MoKα), cm^{-1}	87.6
F(000), *e*	536
hkl range	$-7 \leq h \leq 8$, $-8 \leq k \leq 8$, $-13 \leq h \leq 13$
$((\sin\theta)/\lambda)_{max}$, Å^{-1}	0.715
Reflexions measured	5093
Reflexions unique	218
R_{int}/R_{sigma}	0.118/0.052
Parameters refined	11
$R(F)$[a] ($I > 4\,\sigma(I)$/all data)	0.047/0.051
$wR(F^2)$[b] (all data)	0.106
GoF (F^2)[c]	1.24
$\Delta\rho_{fin}$ (max/min), e Å^{-3}	4.11/−4.01

[a]$R(F) = \Sigma||F_o| - |F_c||/\Sigma|F_o|$; [b]$wR(F^2) = [\Sigma w(F_o^2 - F_c^2)^2/\Sigma w(F_o^2)^2]^{1/2}$; $w = [\sigma^2(F_o^2) + (AP)^2 + BP]^{-1}$, where $P = (Max(F_o^2, 0) + 2F_c^2)/3$; [c]GoF $= S = [\Sigma w(F_o^2 - F_c^2)^2/(n_{obs} - n_{param})]^{1/2}$.

Table 2: Atom positions and displacement parameters (Å^2) with estimated standard deviations in parenthesis. Data of RbTi$_3$Bi$_5$ are from Rietveld fit of the X-ray powder diffraction pattern.

Atom	Wyckoff	*x*	*y*	*z*	U_{eq}
Rb	1*a*	0	0	0	0.027
Cs					0.028(1)
Ti	3*g*	1/2	1/2	1/2	0.013
					0.009(1)
Bi1	4*h*	1/3	2/3	0.2335(4)	0.015
				0.2387(1)	0.013(1)
Bi2	1*b*	0	0	1/2	0.013
					0.011(1)

Table 3: Selected bond lengths (Å) with estimated standard deviations in parenthesis.

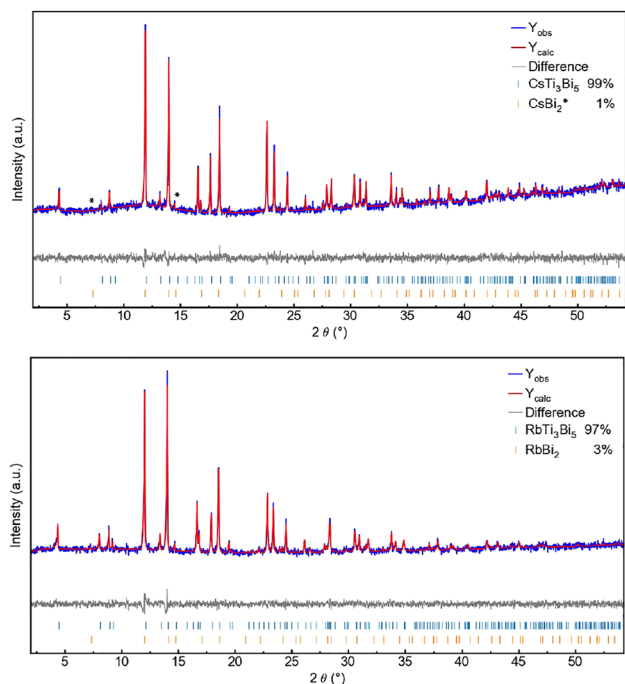|		RbTi$_3$Bi$_5$	CsTi$_3$Bi$_5$
Rb/Cs–Bi1	12×	3.948(2)	3.9990(6)
Ti–Bi1	4×	2.935(3)	2.9290(9)
Ti–Bi2	2×	2.887(1)	2.8937(2)
Ti–Ti	4×	2.887(2)	2.8937(2)
Bi1–Bi1	3×	3.3333(4)	3.3413(2)

Figure 2: X-ray powder patterns (MoKα₁ radiation, blue circles) with Rietveld fits (red) and difference curves (grey) of $CsTi_3Bi_5$ (top) and $RbTi_3Bi_5$ (bottom).

12-fold coordination of cesium. This motif is well known from numerous AlB_2-type compounds [28]. One can thus describe the structure of $CsTi_3Bi_5$ as stacking of $CsBi_4$ layers and planar Ti_3Bi kagomé nets (Figure 3c).

Recently Schoop et al. proposed a scheme to classify kagomé compounds based on geometric and electronic considerations [29]. A tolerance factor $t = \frac{d_K}{d_{NN}}$ is defined where d_K is the bond length within the kagomé network and d_{NN} is the bond length between the atoms of the kagomé network and their nearest neighbors. This gives $t = 0.893$ for $RbTi_3Bi_5$ and $t = 0.988$ for $CsTi_3Bi_5$, respectively. Values ≤ 1.1 indicate that the in-plane bonding is strong, and the band structure is expected to be dominated by the orbitals from the kagomé plane. Such a crystal features an isolated, quasi two-dimensional lattice. Thus, $RbTi_3Bi_5$ and $CsTi_3Bi_5$ fall in the same category as the vanadium compounds AV_3Sb_5 (A = K, Rb, Cs) [19].

2.2 Magnetic and electrical transport properties

Figure 4 shows zero-field cooled magnetic susceptibilities collected under $\mu_0 H = 1$ T external field and magnetization isotherms at T = 1.8 and 300 K for $RbTi_3Bi_5$ and $CsTi_3Bi_5$ single crystals, respectively (inserts). Both compounds
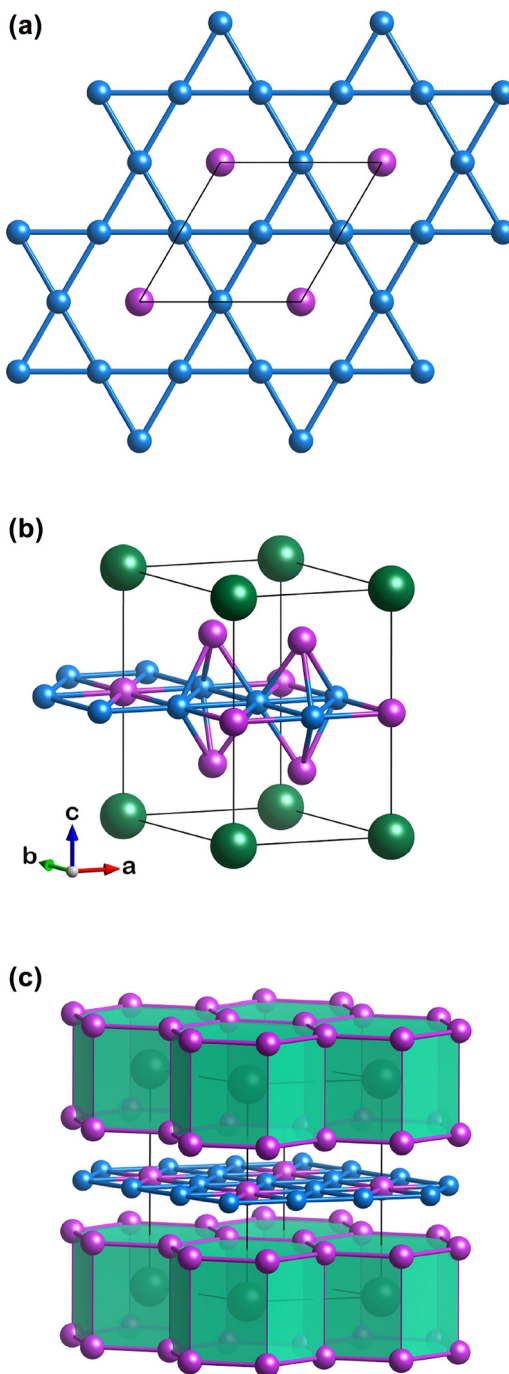

Figure 3: Crystal structure of $CsTi_3Bi_5$ (Cs green, Ti blue, bismuth violet). (a) Kagomé net of titanium atoms with bismuth atoms in the hexagons. (b) Unit cell with additional bismuth atoms above and below the triangles of the kagomé net. (c) Cesium atoms in face-sharing hexagonal prisms of bismuth atoms.

exhibit weak and only slightly temperature-dependent paramagnetism in the order of magnitude of 3.7×10^{-4} emu mol^{-1} Oe^{-1} (1 Oe = 79.6 A m^{-1}) which increases at temperatures below 20 K. The susceptibilities are typical for Pauli paramagnetic metallic materials with traces of local
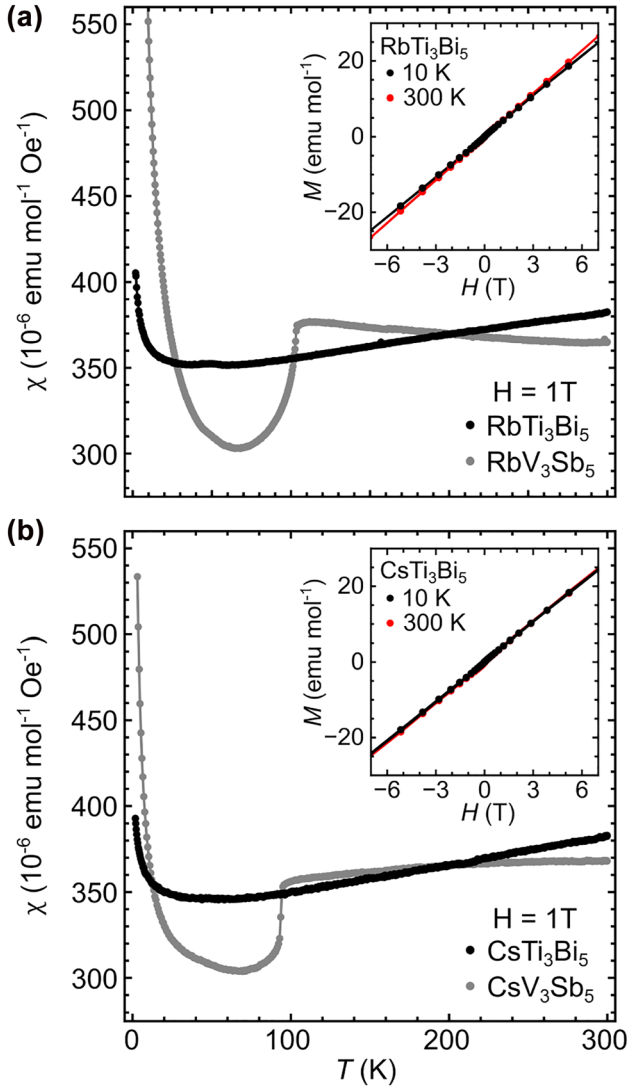
(a)

(b)

Figure 4: Magnetic susceptibilities of $RbTi_3Bi_5$ and $CsTi_3Bi_5$ single crystals at 1 T external field. The inserts show magnetization isotherms at $T = 1.8$ and 300 K. The data for RbV_3Sb_5 and CsV_3Sb_5 are plotted for comparison.

moment paramagnetic impurities, which account for the upturn at low temperatures. The magnetization loops are accordingly linear with increasing field and show no peculiarities (inserts in Figure 4). In Figure 4 we also plot the data for RbV_3Sb_5 and CsV_3Sb_5 for comparison, which exhibit CDW anomalies and structural phase transitions near 90 K. Such anomalies are not visible in the titanium compounds, while the susceptibilities at higher temperatures are similar.

The electrical resistivity of the single crystals with current flowing in the *ab* plane decrease nearly linearly with temperature and saturate towards 3–5 $\mu\Omega$ cm at 1.8 K as expected of metals (Figure 5). Residual resistance ratios
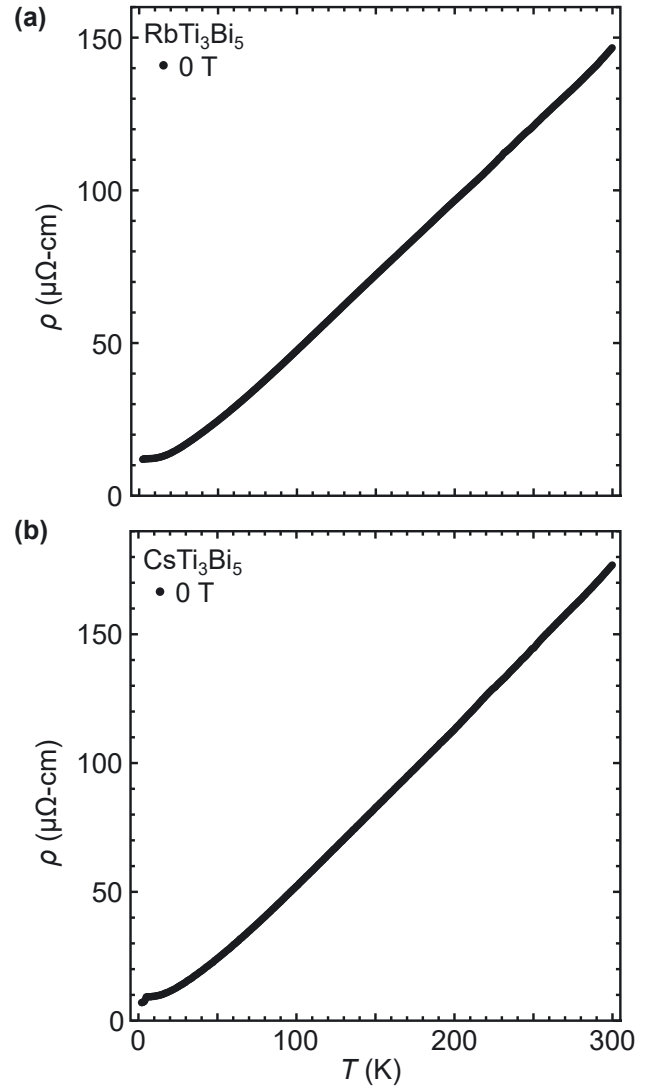
(a)

(b)

Figure 5: In-plane electrical resistivity of $RbTi_3Bi_5$ and $CsTi_3Bi_5$ single crystals at zero external field.

(RRR) are 12 for $RbTi_3Bi_5$ and 18 for $CsTi_3Bi_5$ crystals, respectively. Both materials show weak drops of the resistance near 4 K which reflects small inclusions of a superconducting impurity phase, and no-zero resistivity state was observed. Since we do not detect significant diamagnetism in the low-field susceptibility at 0.5 mT, the trace signatures of superconductivity most likely arise from traces of $RbBi_2$ and $CsBi_2$, respectively, incorporated in the crystals and observed as impurities in the powder samples. The binary Laves phases $RbBi_2$ and $CsBi_2$ are known to be superconducting at 4.21 and 4.65 K, respectively [30, 31], which match the temperatures of the small dips in the resistance. In order to fully rule out possible bulk super-conductivity, we measured the heat capacity of powders. As seen from Figure 6, the heat capacity is featureless and
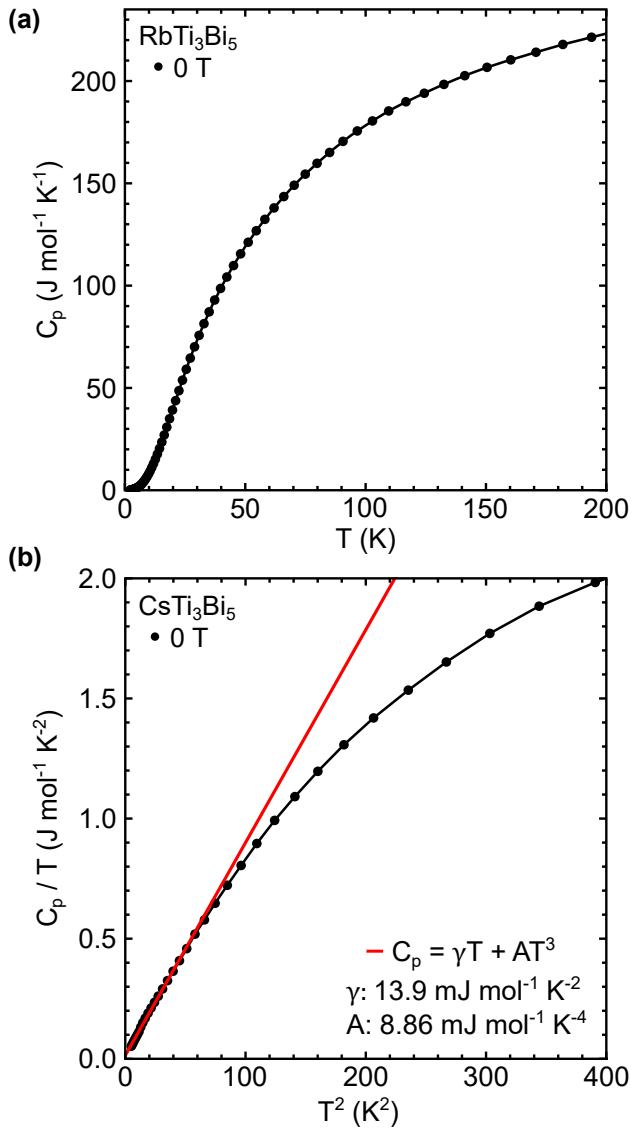
Figure 6: Heat capacity of a RbTi$_3$Bi$_5$ powder compact at zero external field.

saturates to the Dulong-Petit value at room temperature as expected. The Sommerfeld coefficient was extracted from the low temperature data to $\gamma = 13.9$ mJ mol^{-1} K^{-2}.

Like their sister family AV$_3$Sb$_5$, the ATi$_3$Bi$_5$ kagomé metals have exceptionally low resistivities (10–100 μΩ cm) over a wide temperature range, particularly within the *ab* plane. In prior work, we were able to observe quantum oscillations in the magnetoresistance of CsV$_3$Sb$_5$ (Shubnikov-de Haas effect) [27]. With the natural parallel between the VSb and TiBi systems, we turn to look for quantum oscillations in the RbTi$_3$Bi$_5$ system. Figure 7a demonstrates the magnetoresistance of a single crystal of RbTi$_3$Bi$_5$ with current flowing along the *a* axis and the field parallel to the *c* axis. At a 14 T field, the magnetoresistance increases approximately 25% from the zero-field data. Clear signatures of quantum oscillations can be seen in the magnetoresistance. To extract the oscillatory component of the resistivity, we fit a quartic polynomial background function to the resistivity (red curve, Figure 7a). Subtracting the background function yields the purely oscillatory component (Figure 7b). The Fourier transform of the oscillatory data yields a single major frequency at 200 T (Figure 7c). This is a remarkably simple spectra, considering the relative complexity of the band structure. Observation of many of the higher frequency orbits may be limited due to the lower RRR in the Ti-Bi family and any additional complexities due to air sensitivity.

2.3 Electronic band structure

The electronic structure of CsTi$_3$Bi$_5$ was calculated from first principles using the Vienna *Ab initio* Simulation Package (VASP). Figure 8 shows the total and atom-projected density of states (DOS) of CsTi$_3$Bi$_5$ together with the one of CsV$_3$Sb$_5$ for comparison.
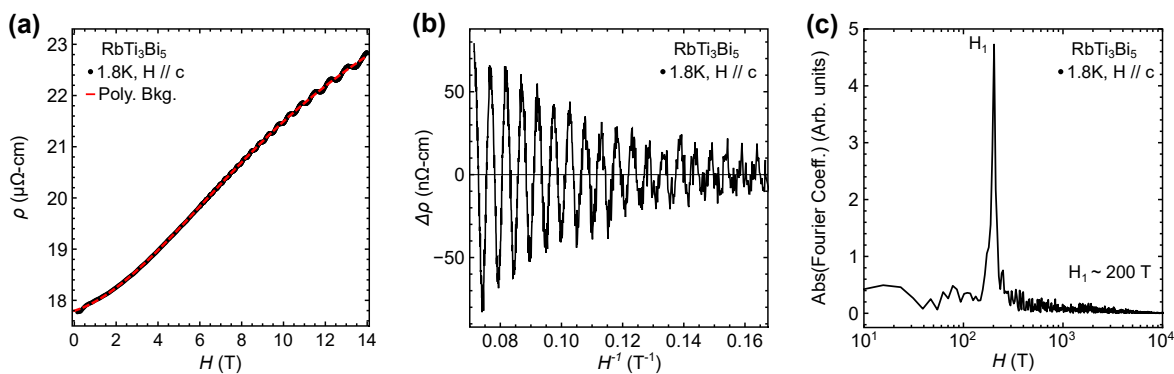

Figure 7: Magnetoresistance measurements (a) on RbTi$_3$Bi$_5$ at 1.8 K show clear signatures of quantum oscillations (Shubnikov-de Haas effect). Utilizing a quartic polynomial to subtract off the background resistance, we isolate the oscillatory component of the magnetoresistance (b) and perform Fourier analysis (c) to identify a dominant frequency ($H_1 \sim 200$ T).

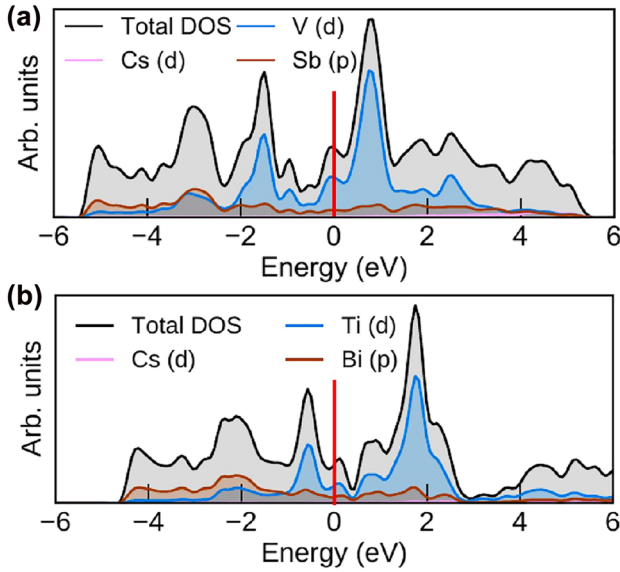**Figure 8:** Electronic total and projected density of states for CsV_3Sb_5 (a) and $CsTi_3Bi_5$ (b).

Both DOS patterns are similar and mainly differ by the position of the Fermi level, which is much lower in the case of $CsTi_3Bi_5$. This is as expected, because it has three electrons less per unit cell the thus the band filling is much lower. The effect mainly relates to $3d$ bands (blue shaded areas), which have the largest contributions around the Fermi energy. The band structure of $CsTi_3Bi_5$ is strongly affected by spin-orbit coupling due to the heavy element bismuth. Figure 9 shows the band structure of $CsTi_3Bi_5$ with spin orbit coupling included.

Symmetry analysis of the band structure has characterized the vanadium compounds AV_3Sb_5 (A = K, Rb, Cs) as $\mathbb{Z}_2$ topological metals [21, 22]. In these V-based kagomé systems, the presence of continuous gaps between the

bands near the Fermi level permitted the $\mathbb{Z}_2$ topological classification via wave function parity product calculations at the time-reversal invariant momentum (TRIM) points in the Brillouin zone [32]. $CsTi_3Bi_5$ likewise possesses time-reversal and inversion symmetry necessary for this $\mathbb{Z}_2$ calculation method, however, analysis of the electronic structure of $CsTi_3Bi_5$ using a higher k-point density and considering the band symmetries between the high symmetry points indicate that relevant bands (red, magenta, light blue in Figure 9) exhibit symmetry-enforced crossings between the Γ_7/Γ_8 bands (red, light blue) and the Γ_8/Γ_9 bands (red, magenta) between the Γ and A points. Given these crossings and the subsequent absence of continuous gaps, the $\mathbb{Z}_2$ topological invariant cannot be calculated using parity products at the TRIM points. Further analysis of the nature of these band crossings is necessary to categorize the electronic structure of $CsTi_3Bi_5$ as topologically trivial or not.

3 Experimental section

3.1 Synthesis

Due to the air sensitivity of the powders and crystals, all measurement preparation was performed in an argon glovebox with water and oxygen levels <0.5 ppm.

Polycrystalline samples of $RbTi_3Bi_5$ and $CsTi_3Bi_5$ were synthesized by heating stoichiometric mixtures of the elements (Rb, ingot, Alfa 99.75%; Cs, liquid, Smart-elements 99.98%; Ti, powder, Alfa 99.5%; Bi, coarse powder, Sigma-Aldrich 99.999%) in alumina crucibles welded in silica ampoules under an atmosphere of purified argon. Both $RbTi_3Bi_5$ and $CsTi_3Bi_5$ are grey crystalline powders interspersed with platelet silver crystals (up to $0.12 \times 0.12 \times 0.04$ mm^3) after being sintered at 600 °C for 48 h and subsequently cooled at a rate of 20 K h^{-1}. Single crystals of $RbTi_3Bi_5$ and $CsTi_3Bi_5$ were synthesized using a self-flux with a method and composition similar to that published previously [27]. Specifically we created a precursor phase by ball milling elemental Bi shot (Alfa, 99.999%), Ti powder (Alfa, 99.9%), and Cs liquid (Alfa, 99.98%) at a molar ratio of approximately 1:1:6. This precursor was loaded into CoorsTek 2 mL high-density high-purity alumina crucibles and sealed in either: 1) carbon-coated silica ampoules sealed under 0.5 atm argon, or 2) steel tubes sealed under 1 at. argon. Fluxes are heated to 900 °C at a rate of 200 K h^{-1}, held at 900 °C for 12 h, and cooled to 450–500 °C at a rate of 3 K h^{-1} before molten flux was removed through centrifugation. Crystals form as hexagonal plates with typical dimensions of up to 1 cm $\times$ 1 cm $\times$ 0.25 mm. They are malleable, readily exfoliated, and mechanically similar to the AV_3Sb_5 family. However, unlike AV_3Sb_5, crystals are extremely sensitive to air and water, and freshly cleaved surfaces will tarnish irreversibly in the order of 1 min. Tarnished layers do not protect against additional damage, and degradation will proceed throughout the entire crystal over the course of a few hours.
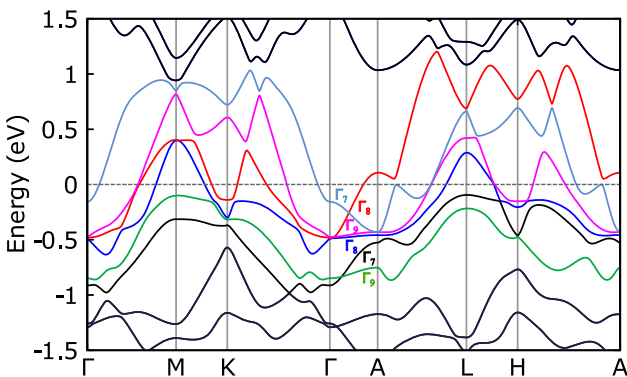

Figure 9: Electronic band structure of $CsTi_3Bi_5$ with spin orbit coupling. The symmetry labels at along Γ-A mark symmetry-enforced crossings so that these bands cannot form a gap.

3.2 Crystal structure determinations

The crystal structure of $CsTi_3Bi_5$ was determined by single-crystal X-ray diffraction using a Bruker D8 Quest diffractometer with a fixed χ-goniometer, MoKα radiation and a Photon 100 detector. Data was acquired using the Apex3 software [33]. The structure was refined using SHELXL [34]. X-ray Powder diffraction data was measured on a STOE Stadi-P diffractometer using a MoKα source and a Dectris Mythen 1K strip detector. Powders were diluted in a mass ratio of 1:5 with ground amorphous glass and sealed in glass capillaries (d = 0.1 mm). The structure data of $CsTi_3Bi_5$ were used as starting parameters for Rietveld fits with TOPAS V4.1 [35].

Further details of the crystal structure investigation may be obtained from Fachinformationszentrum Karlsruhe, 76344 Eggenstein-Leopoldshafen, Germany (Fax: +49-7247-808-666; E-mail: crysdata@fiz-karlsruhe.de, http://www.fiz-informationsdienste.de/en/DB/icsd/depot_anforderung.html) on quoting the deposition numbers CSD 2208937 ($CsTi_3Bi_5$) and CSD 2208938 ($RbTi_3Bi_5$).

3.3 Magnetization measurements

Magnetization measurements were performed on a Quantum Design MPMS3 using vibrating sample magnetometry (VSM). Superconductivity tests were performed under a 5 Oe applied field, while general screening for other magnetic properties was performed at 1 T. Powder samples were loaded in polypropylene capsules, sealed with a thin layer of PARAFILM®. Crystals were mounted onto quartz paddles with small quantities of GE varnish. Resistivity and quantum oscillation measurements were performed on a Quantum Design Dynacool 14T system using the electrical transport option (ETO) with a probe current of 5 mA and frequency of ~100 Hz. Crystals were cleaved, exfoliated, and mounted to the resistivity stage within the glovebox. Contacts were made using silver paint (DuPont cp4929N-100) and gold wire (Alfa, 0.05 mm premion 99.995%). Heat capacity measurements were performed on a Quantum Design Dynacool 9 T system using the heat capacity option. Sections of a sintered powder compact were adhered to the sample stage using a small quantity of Apezion N grease.

3.4 Computations

The electronic structure of $CsTi_3Bi_5$ was calculated from first principles using the Vienna *Ab initio* Simulation Package (VASP, version 5.4.4) [36–38] based on density functional theory and plane wave basis sets. These calculations employed the PBE functional with D3 corrections to account for the van-der-Waals forces along the c axis in $CsTi_3Bi_5$ [39]. Projector-augmented wave (PAW) pseudopotentials [40] were selected based on the VASP 5.4 recommendations. The plane wave energy cutoff was set to 520 eV and a $23 \times 23 \times 11$ Γ-centered k-mesh was automatically generated within VASP using the Monkhorst-Pack method [41]. The structure was relaxed with a force cutoff of 10^{-3} eV Å^{-1}. All calculations were performed with spin-orbit coupling and an energy convergence better than 10^{-7} eV. The k-point path for the band structure (Figure 9) was generated using SUMO-KGEN [42] and contains 1899 k-points.

Author contributions: All the authors have accepted responsibility for the entire content of this submitted manuscript and approved submission.

Conflict of interest statement: The authors declare no conflicts of interest regarding this article.

Note added: During the preparation of this manuscript, we recognized unpublished preprints about $CsTi_3Bi_5$ (https://arxiv.org/abs/2209.03840, https://arxiv.org/abs/2202.05588).

References

1. Grey I. E. *Mineral. Mag.* 2020, *84*, 640–652.
2. Stein F., Leineweber A. *J. Mater. Sci.* 2021, *56*, 5321–5427.
3. Syôzi I. *Prog. Theor. Phys.* 1951, *6*, 306–308.
4. Anderson P. W. *Mater. Res. Bull.* 1973, *8*, 153–160.
5. Sachdev S. *Phys. Rev. B* 1992, *45*, 12377–12396.
6. Anderson P. W. *Science* 1987, *235*, 1196–1198.
7. Hiroi Z., Ishikawa H., Yoshida H., Yamaura J.-I., Okamoto Y. *Inorg. Chem.* 2019, *58*, 11949–11960.
8. Gingras M. J. P., Stager C. V., Raju N. P., Gaulin B. D., Greedan J. E. *Phys. Rev. Lett.* 1997, *78*, 947–950.
9. Shores M. P., Nytko E. A., Bartlett B. M., Nocera D. G. *J. Am. Chem. Soc.* 2005, *127*, 13462–13463.
10. Helton J. S., Matan K., Shores M. P., Nytko E. A., Bartlett B. M., Yoshida Y., Takano Y., Suslov A., Qiu Y., Chung J. H., Nocera D. G., Lee Y. S. *Phys. Rev. Lett.* 2007, *98*, 107204.
11. Okamoto Y., Nohara M., Aruga-Katori H., Takagi H. *Phys. Rev. Lett.* 2007, *99*, 137207.
12. Mendels P., Bert F., de Vries M. A., Olariu A., Harrison A., Duc F., Trombe J. C., Lord J. S., Amato A., Baines C. *Phys. Rev. Lett.* 2007, *98*, 077204.

13. Depenbrock S., McCulloch I. P., Schollwöck U. *Phys. Rev. Lett.* 2012, *109*, 067201.
14. Yan S., Huse D. A., White S. R. *Science* 2011, *332*, 1173–1176.
15. Broholm C., Cava R. J., Kivelson S. A., Nocera D. G., Norman M. R., Senthil T. *Science* 2020, *367*, eaay0668.
16. Guo H. M., Franz M. *Phys. Rev. B* 2009, *80*, 113102.
17. O'Brien A., Pollmann F., Fulde P. *Phys. Rev. B* 2010, *81*, 235115.
18. Wang W.-S., Li Z.-Z., Xiang Y.-Y., Wang Q.-H. *Phys. Rev. B* 2013, *87*, 115135.
19. Ortiz B. R., Gomes L. C., Morey J. R., Winiarski M., Bordelon M., Mangum J. S., Oswald L. W. H., Rodriguez-Rivera J. A., Neilson J. R., Wilson S. D., Ertekin E., McQueen T. M., Toberer E. S. *Phys. Rev. Mater.* 2019, *3*, 094407.
20. Jiang Y. X., Yin J. X., Denner M. M., Shumiya N., Ortiz B. R., Xu G., Guguchia Z., He J. Y., Hossain M. S., Liu X. X., Ruff J., Kautzsch L., Zhang S. T. S., Chang G. Q., Belopolski I., Zhang Q., Cochran T. A., Multer D., Litskevich M., Cheng Z. J., Yang X. P., Wang Z. Q., Thomale R., Neupert T., Wilson S. D., Hasan M. Z. *Nat. Mater.* 2021, *20*, 1353–1357.
21. Ortiz B. R., Sarte P. M., Kenney E. M., Graf M. J., Teicher S. M. L., Seshadri R., Wilson S. D. *Phys. Rev. Mater.* 2021, *5*, 034801.
22. Ortiz B. R., Teicher S. M. L., Hu Y., Zuo J. L., Sarte P. M., Schueller E. C., Abeykoon A. M. M., Krogstad M. J., Rosenkranz S., Osborn R., Seshadri R., Balents L., He J. F., Wilson S. D. *Phys. Rev. Lett.* 2020, *125*, 247002.
23. Yang S. Y., Wang Y. J., Ortiz B. R., Liu D. F., Gayles J., Derunova E., Gonzalez-Hernandez R., Smejkal L., Chen Y. L., Parkin S. S. P., Wilson S. D., Toberer E. S., McQueen T., Ali M. N. *Sci. Adv.* 2020, *6*, eabb6003.
24. Oey Y. M., Kaboudvand F., Ortiz B. R., Seshadri R., Wilson S. D. *Phys. Rev. Mater.* 2022, *6*, 074802.

25. Oey Y. M., Ortiz B. R., Kaboudvand F., Frassineti J., Garcia E., Cong R., Sanna S., Mitrović V. F., Seshadri R., Wilson S. D. *Phys. Rev. Mater.* 2022, *6*, L041801.
26. Jiang Y., Yu Z., Wang Y., Lu T., Meng S., Jiang K., Liu M. *Chin. Phys. Lett.* 2022, *39*, 047402-1-047402-7.
27. Ortiz B. R., Teicher S. M. L., Kautzsch L., Sarte P. M., Ratcliff N., Harter J., Ruff J. P. C., Seshadri R., Wilson S. D. *Phys. Rev. X* 2021, *11*, 041030.
28. Hoffmann R.-D., Pöttgen R. *Z. Kristallogr.* 2001, *216*, 127–145.
29. Jovanovic M., Schoop L. M. *J. Am. Chem. Soc.* 2022, *144*, 10978–10991.
30. Li H., Ikeda M., Suzuki A., Taguchi T., Zhang Y., Goto H., Eguchi R., Liao Y.-F., Ishii H., Kubozono Y. *Phys. Chem. Chem. Phys.* 2022, *24*, 7185–7194.
31. Roberts B. W. *J. Phys. Chem. Ref. Data* 1976, *5*, 581–821.
32. Fu L., Kane C. L. *Phys. Rev. B* 2007, *76*, 045302.
33. *Apex3, Data Reduction and Frame Integration Program for the CCD Area-Detector System*; Bruker AXS Inc.: Madison, Wisconsin (USA), 2016.
34. Sheldrick G. M. *Acta Crystallogr.* 2008, *A64*, 112–122.
35. Coelho A. *Topas-Academic (version 4.1)*; Coelho Software: Brisbane (Australia), 2007.
36. Kresse G., Furthmüller J. *Comput. Mater. Sci.* 1996, *6*, 15–50.
37. Kresse G., Furthmüller J. *Phys. Rev. B* 1996, *54*, 11169–11186.
38. Kresse G., Hafner J. *Phys. Rev. B* 1993, *47*, 558–561.
39. Grimme S., Antony J., Ehrlich S., Krieg H. *J. Chem. Phys.* 2010, *132*, 154104.
40. Kresse G., Joubert D. *Phys. Rev. B* 1999, *59*, 1758–1775.
41. Monkhorst H. J., Pack J. D. *Phys. Rev. B* 1976, *13*, 5188–5192.
42. Ganose A. M., Jackson A. J., Scanlon D. O. *J. Open Source Software* 2018, *3*, 717.